Experimentally informed fracture modelling of interfacial transition zone at micro-scale

Zhang, Hongzhi; Gan, Yidong; Xu, Yading; Zhang, Shizhe; Schlangen, Erik; Šavija, Branko

DOI
10.1016/j.cemconcomp.2019.103383

Publication date
2019

Document Version
Final published version

Published in
Cement and Concrete Composites

Citation (APA)
Zhang, H., Gan, Y., Xu, Y., Zhang, S., Schlangen, E., & Šavija, B. (2019). Experimentally informed fracture modelling of interfacial transition zone at micro-scale. *Cement and Concrete Composites*, *104*, Article 103383. https://doi.org/10.1016/j.cemconcomp.2019.103383

Cement and Concrete Composites 104 (2019) 103383

Contents lists available at ScienceDirect

Cement and Concrete Composites

journal homepage: www.elsevier.com/locate/cemconcomp

Experimentally informed fracture modelling of interfacial transition zone at micro-scale

Hongzhi Zhang, Yidong Gan*, Yading Xu, Shizhe Zhang, Erik Schlangen, Branko Šavija

Faculty of Civil Engineering and Geosciences, Delft University of Technology, 2628 CN, Delft, the Netherlands

A B S T R A C T

The aim of this work is to predict the micromechanical properties of interfacial transition zone (ITZ) by combining experimental and numerical approaches. In the experimental part, hardened cement paste (HCP) cantilevers (200 μm × 100 μm × 100 μm) attached to a quartzite aggregate were fabricated and tested using micro-dicing saw and nanoindenter, respectively. In the modelling, comparable digital specimens were produced by the X-ray computed tomography (XCT) and tested by a discrete lattice model. The fracture model was calibrated by the experimental load-displacement curves and can reproduce the experimental observations well. In the end, the calibrated model was used to predict the mechanical behaviour of ITZ under uniaxial tension, which can be further used as input for the multi-scale analysis of concrete.

1. Introduction

Concrete is the dominant construction material in the world [1]. It is a composite material consisting of cement paste and aggregate inclusions with various particle sizes. Between cement paste and aggregates, a thin layer with properties different from the bulk paste forms [2–6]. This layer is known as the interfacial transition zone, with a thickness between 30 and 80 μm. This layer has a different porosity, phase composition, and density compared to the bulk paste. As such, it is believed that the ITZ has inferior mechanical and transport properties compared to the bulk paste [6–12]. Therefore, it plays a dominant role in determining the overall performance of this composite material.

Concrete is generally considered to be a three-phase material composed of aggregate, cement paste matrix and the ITZ at meso-scale [13–19]. In order to offer fundamental insight into the fracture mechanisms of such composite material and give a proper prediction, the input parameters of each phase are required to be calibrated separately. The behaviour of the matrix phase and the aggregate can be studied in a rather straightforward manner because these materials can be prepared and tested individually. Unfortunately, this does not apply to the ITZ, because this zone is an integral part of the whole microstructure together with the bulk cement paste and the aggregate [20]. Over the past decades, various test configurations have been developed to study the interface fracture at the meso-scale. The specimens are generally made by casting the cementitious matrix against a flat block of aggregate. Load is then applied to split these two materials along the interface to quantify the bonding strength. Mode I and mode II are the mostly adopted loading conditions for the mechanical properties measurements. The mode I loading types include the uniaxial tensile test [21–23], wedge splitting [24,25], flexure test (i.e. cantilever bending [26,27] and three-point bending [28–30]) and Brazilian splitting test [29], while mode II experiments contain mainly push-out test [31,32] and slant shear test [33]. Based on these aforementioned techniques, a lot of knowledge about the influence of ITZ on the mechanical performance of concrete has been gained. However, almost all fracture experiments are carried out at the scales larger than that of real aggregate in concrete. A clear understanding about the micromechanical properties of the ITZ is still missing, as it is a special material feature at the micro-scale. At this scale, studies are mostly carried out by simulations [34–36] due to the technical and instrumental limitations. Consequently, these models cannot be validated due to the mismatch in terms of the investigated scale length. Therefore, there is a need for experimental measurements at the micro-scale, which can be used for the calibration and validation of the micromechanical modelling of the ITZ.

Recent reports document the utilization of nanoindenter as a versatile instrument for loading micrometre sized specimens [37–43]. The specimens can be prepared either by a focused ion beam (FIB) milling technique [37–39] or physical micro-dicing procedure [40–43]. The FIB milling technique uses a focused Ga-ion beam for precise micro-machining of various materials to fabricate specimens with designed geometries, typically the micro-cantilever [37,38] and micro-pillar [39]. However, considering the relatively low milling efficiency, the size of the machined specimen is generally limited up to 10 μm, which is not large enough to represent the HCP matrix but for a single phase in

* Corresponding author.
E-mail addresses: h.zhang-5@tudelft.nl (H. Zhang), Y.Gan@tudelft.nl (Y. Gan), Y.Xu-5@tudelft.nl (Y. Xu), Shizhe.Zhang@tudelft.nl (S. Zhang), erik.schlangen@tudelft.nl (E. Schlangen), b.savija@tudelft.nl (B. Šavija).

https://doi.org/10.1016/j.cemconcomp.2019.103383
Received 27 March 2019; Received in revised form 1 July 2019; Accepted 30 July 2019
Available online 31 July 2019
0958-9465/

the matrix. The micro-dicing technique developed by the authors has proved to be able to produce specimens with a size of a few hundred micrometres with shape of cube, prism and cantilever beam [42–44]. This technique is therefore adopted to produce small HCP cantilevers having one end bonded to the aggregate. To test the fracture performance of aggregate-cement interface, a load was applied at the free end of the cantilever by the nanoindenter. To the authors' best knowledge, it is the first time that fracture of aggregate-cement interface has been successfully tested at the micro-scale. This offers valuable experimental data for the calibration and validation of the micromechanical modelling of the ITZ.

In addition to experiments, a micromechanical model of ITZ is proposed. The model is built up on the basis of a combination of X-ray computed tomography and discrete lattice fracture model. It is first calibrated by the experimental results and further used to predict the micromechanical properties of the pure ITZ. This work presents a fundamental study of the fracture testing and modelling of the aggregate-cement interface at the micrometre length scale. The predicted micromechanical properties of ITZ can be further used to determine the interface properties between aggregate and HCP in the discrete fracture modelling of concrete or mortar at the meso-scale.

2. Experimental

2.1. Materials and sample preparation

For the sample preparation, standard CEM I 42.5 N Portland cement, quartzite aggregate and deionized water were used. A flat aggregate slice having thickness of 1 mm was made by cutting and thin-sectioning. The procedure is the same as that used for preparation of concrete thin sections. As aggregates are harder than cement paste, it was assumed that the damage caused to the aggregates during this procedure is negligible.[1] The thin-sectioning was conducted by grinding using a Struers Labopol-5 thin sectioning machine. To obtain smooth and parallel surfaces and to eliminate the effect of different surface roughness, both sides were ground using discs with grit sizes of 135 μm and 35 μm in a descending order. The slice was placed at the bottom of a plastic mould. Fresh cement paste with w/c ratio of 0.3 was mixed following EN 196–3:2005 + A1:2008 (E) using a Hobart mixer and cast on the top of the aggregate slice. After 28 days curing under sealed conditions, the HCP-aggregate specimen was demoulded. A thin-sectioning procedure was then conducted on the HCP surface to make the thickness of the whole specimens 1.2 mm (0.2 mm cement paste layer and 1 mm aggregate layer, see Fig. 1a). To fabricate micrometre sized cement paste cantilever having one end attached to the aggregate, the following steps as shown in Fig. 1 were conducted using a micro-dicing saw which is originally used for the microchip industry with a dicing tolerance down to a few micrometres. This ensures the precision for preparing specimens with size of a few hundred micrometres. The blade was run in two perpendicular directions as shown in Fig. 1b and c to fabricate the HCP beam with a square cross-section of 100 μm and a length of 200 μm on the aggregate. The dicing width was set as the sum of the length of the designed cross-section (100 μm) and the thickness of the blade (260 μm). The blade was cut 20 μm into the aggregate in order to have a clear boundary between HCP beam and the aggregate support. A strip of aggregate consisting of a row of HCP cantilevers was then cut off from the aggregate slice as shown in Fig. 1d. Afterwards, the morphology of the produced cantilever beams were checked by an environmental scanning electron microscope (ESEM) under the back-scattered electron (BSE) mode, see Fig. 2. A clear boundary with much higher porosity between the HCP beam and aggregate support can be clearly observed in Fig. 2c, indicating a weak bound between the HCP and aggregate.

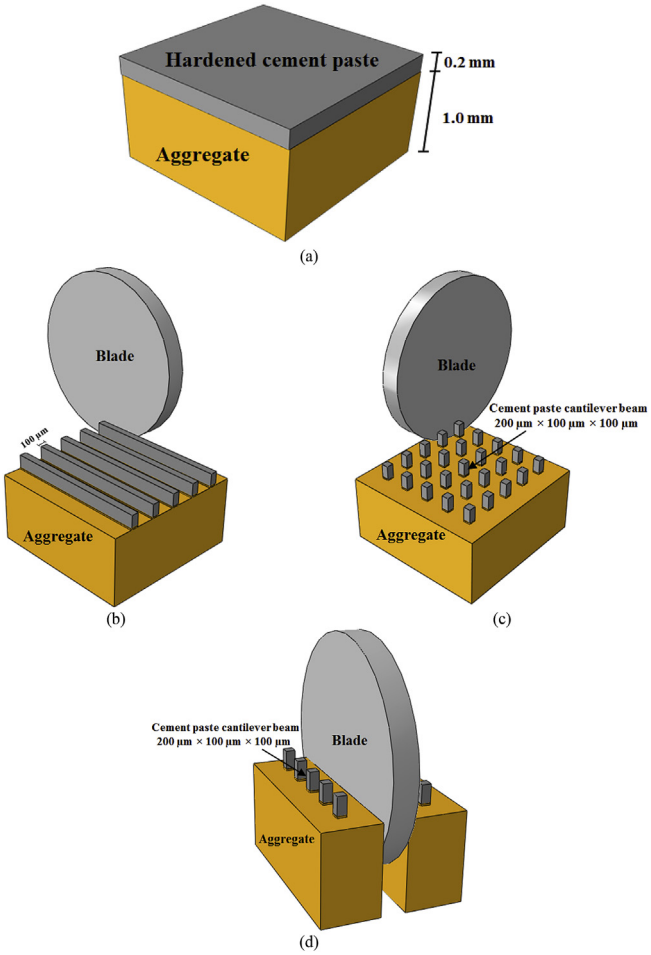

Fig. 1. Schematic illustration of the sample preparation procedure: (a) preparing a HCP-aggregate slice; (b) cutting through HCP at one direction; (c) cutting through HCP at a perpendicular direction; (d) cutting one aggregate strip off.

2.2. Fracture test using nanoindenter

The test configuration is schematically shown in Fig. 3. The aggregate strip was attached to a support vertically resulting in a row of HCP cantilevers standing horizontally. A nanoindenter was then instrumented for applying load at the free end of the cantilever. To eliminate the possible penetration of the indenter into the specimen, a commercialised flat end cylindrical tip with a diameter of 330 μm was adopted instead of a standard Berkovich tip. The tip was set to be aligned with the centre of the free end of the beam using the in-situ imaging system. To ensure the positioning accuracy, a microscope to indenter calibration procedure was conducted prior to the test. The test was run under a displacement-controlled method with a constant displacement increment of 50 nm per second. The cantilever beams were loaded until failure and the load-displacement curves were recorded by the nanoindenter for further analysis.

2.3. Experimental results

In total, 10 cantilever beams were tested. Fig. 4 shows their load-displacement curves. A good repeatability can be found and, in general, these curves can be divided into two parts: ascending and plateau. In

[1] In the current study, possible damage caused to the aggregate by the specimen preparation procedure can certainly be neglected. As shown by the experimental results, the micro-cantilevers have always failed in the cement paste part (ITZ), and not in the aggregate part.

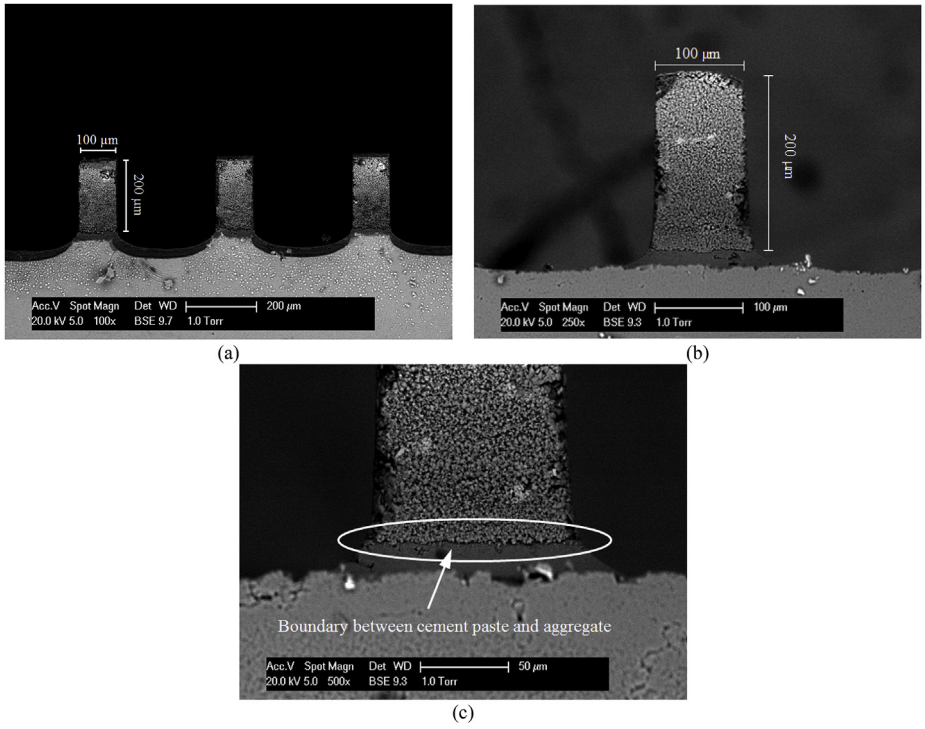

Fig. 2. ESEM micrographs of (a) a row of cantilever beams, (b) one cantilever beam (dimension shown) and (c) the interface between HCP beam and the aggregate.

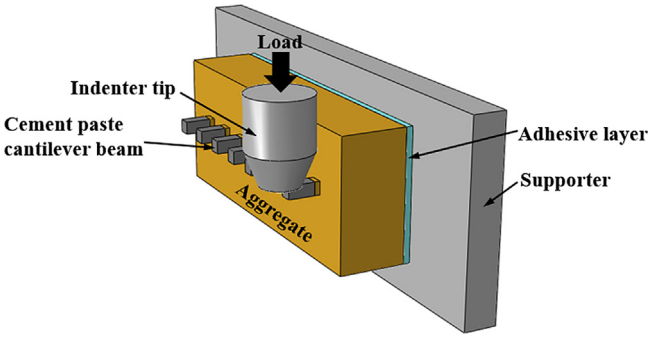

Fig. 3. Schematic view of the micro-cantilever mechanical test setup.

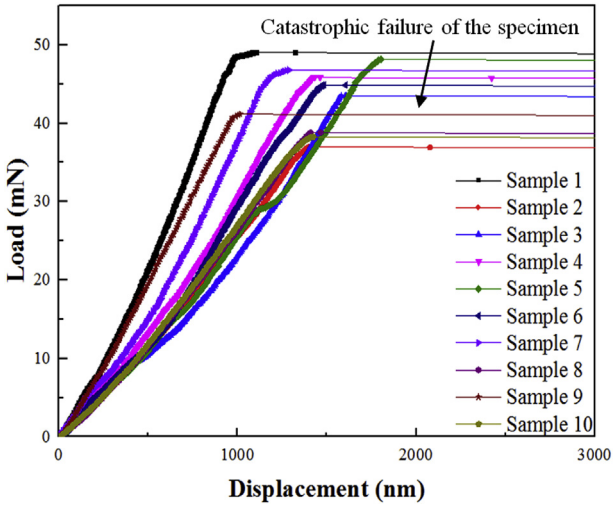

Fig. 4. Measured load-displacement curves of ITZ cantilever beams subjected to bending.

the ascending part, the load increases monotonically with the displacement until reaches a critical load. Afterwards, a displacement jump is observed. It must be emphasised that the plateau in the curves does not correspond to the material behaviour, but a catastrophic failure of the specimen. This is because the control of the nanoindenter is not fast enough to enable a measurement of the post-peak behaviour. Consequently, the indenter overshoots downward before the load decreasing. Thus, only the first regime was used for the calibration of the fracture model in Section 4.2. In this regime, the peak load ranging from 36.96 mN to 49.03 mN and its corresponding displacement (1103.6–1432.62 nm) can be derived. The fluctuation is mainly attributed to the heterogeneous nature of the material structure, especially the porous interface. Note that these values cannot be used to calculate the interface properties through simple analytical solutions for bending or shearing because of the complex boundary conditions at the interface introduced by the test configuration. In this case, the numerical approach shows advantages when dealing with such complex boundary conditions.

After the fracture test, the aggregate strip was checked by the ESEM. Fig. 5 shows the remaining aggregate support. This means that the crack occurs along the interface between the aggregate and HCP. A top view of the fractured surface is shown in Fig. 6. It can be distinguished from the texture of the surface that part of HCP remains on the aggregate surface, indicating a tortuous fracture surface. This agrees well with the macroscopic observations [45].

3. Digital specimens

3.1. XCT experiments

The fracture modelling requires virtual specimen with details of the featured material structure. In this work, X-ray computed tomography (XCT) and image segmentation techniques were used to characterize the material structure and build the digital specimens which are comparable with the realistic specimen. A HCP-aggregate prism was created and clamped on a special holder for the scanning. A small drop of cyanoacrylate adhesive was added to the surface of the specimen to

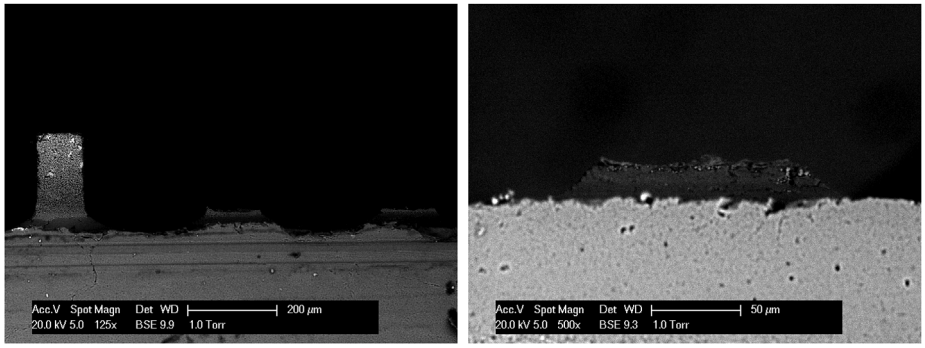

(a) (b)

Fig. 5. ESEM micrographs of the ITZ cantilever beams after failure: (a) an intact cantilever and two fractured cantilevers (b) remains of the microcantilever after failure (higher magnification).

protect the sample from breaking during clamping. The prism has a square cross-section of 500 μm × 500 μm and a length of 3 mm. It was fabricated using a similar approach as proposed in Section 2.1. First, a 3 mm two-layer cement paste-aggregate material (2 mm aggregate substrate and 1 cement paste layer) was made by casting cement paste on a 2 mm aggregate slice and grinding after 28 days curing. The micro-dicing saw was then run two perpendicular directions over the slice to create the prisms. In order to separate these prisms, the saw was set to cut through the aggregate during the dicing.

In the XCT experiment, the holder was fixed in the rotatable stage. The X-ray source tube was set as 120 Kev/60 μA for the scanning. 2800 projections were acquired using a digital GE DXR detector (3072 × 2400 pixels). This setup results in a greyscale level-based material structure with a resolution of 1 μm × 1 μm × 1 μm. In order to reduce the noise in the reconstructed XCT images as well as the computational efforts in the discrete fracture modelling, a binning level of 2 was used in the reconstruction. The resulted final material structure has a resolution of 2 μm × 2 μm × 2 μm. Afterwards, a stack of 2D slices from the side view was exported for image segmentation and digital specimen generation. To reduce the influence of beam hardening in the XCT experiment, a region of interest (ROI) with a cross-section of 300 μm × 300 μm and length of 1000 μm was extracted from the central region of the scanned specimen.

3.2. Microstructure characterisation

In general, aggregate particles are observed as relatively homogeneous in X-ray CT images. On the other hand, cement paste shows significant heterogeneity due to presence of porosity and different hydration phases. Therefore, differences in relative grayscale levels can be used to distinguish between the aggregate and the paste phase in X-ray CT images. This was also done in the current study. First, the deviation of greyscale level along the height of the ROI was analysed by calculating the coefficient of variation (CoV):

$$\mathrm{CoV_i} = \frac{S_\mathrm{i}}{\mu_\mathrm{i}} \tag{1}$$

where $\mathrm{CoV_i}$ is the CoV of greyscale level at height i, S_i the standard deviation greyscale level at height i, μ_i the mean greyscale level at height i. As shown in Fig. 7, on the one hand, the CoV at the aggregate part is relatively low (around 0.05). On the other hand, HCP has a much higher CoV. It is therefore reasonable to consider the aggregate as a single-phase material in the model. Note that the CoV value at height i is averaged from the 3D ROI rather than a 2D slice. Additionally, a significant increase of CoV (from 0.05 to 0.25) is observed at the boundary between the aggregate and HCP, which was used to separate the two materials from the original greyscale level-based images.

To consider the heterogeneity of HCP at the micro-scale, both the continuous greyscale level based material structure [46] and multi-phase based material structure [42] can be used. Herein, a global thresholding approach that developed in the authors' previous work was adopted to segment the HCP part into a 4-phase material consisting of capillary pore (CP), inner hydration product (IHP), outer hydration product (OHP) and anhydrous cement particle (ACP). This method determines the threshold value of greyscale value using both cumulative and histogram of the greyscale level in the ROI. In order to avoid the influence of the ITZ on the determination of the threshold value of different phases, the region away from the boundary of 150 μm was used, which can be regarded as the bulk cement paste. More details of this approach can be found in Ref. [42]. The information of the segmented material structure of bulk cement paste is listed in Table 1, which is similar to the results that obtained by the authors for a pure

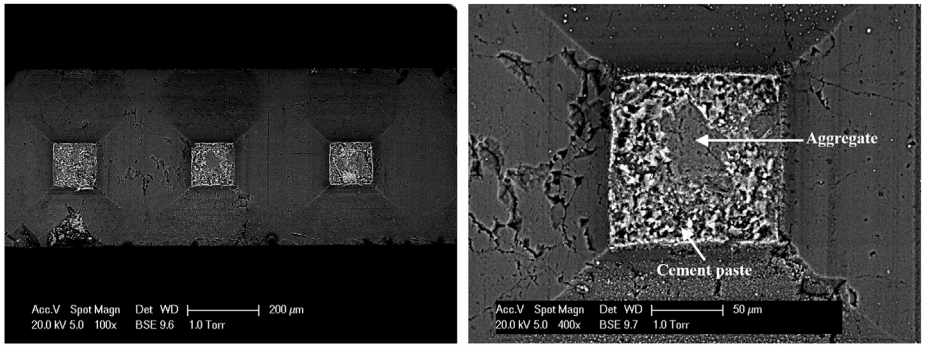

(a) (b)

Fig. 6. ESEM micrographs of the fracture surface after ITZ cantilever beam failure: (a) three fracture cantilevers (b) one cracked surface at higher magnification.

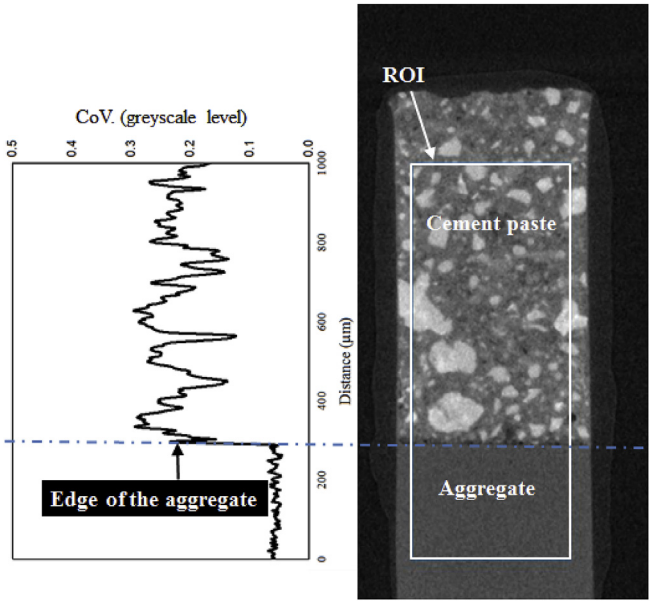

Fig. 7. (left) CoV of the greyscale level along the ROI, clearly indicating a more homogeneous GSV distribution in the aggregate compared to paste; (right) A slice from the X-ray CT micrograph of the cement paste/aggregate specimen (Both shown in 2D for clarity).

Table 1
Information of the segmented bulk cement paste.

Porosity	Anhydrous cement particles	Hydration degree
8.35%	16.96%	66.69%

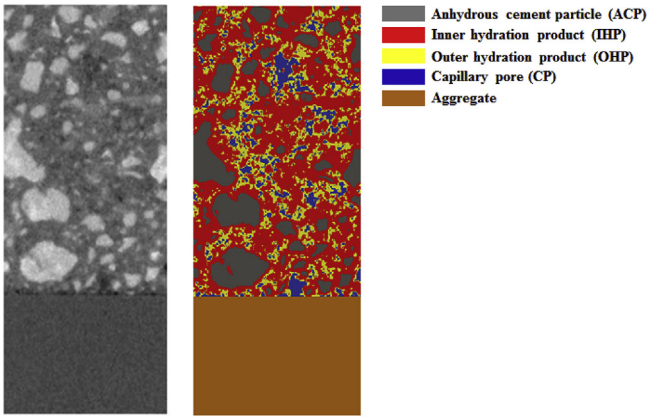

Fig. 8. (Left) X-ray computed tomography of the ROI; (right) segmented microstructure of the ROI (Both shown in 2D for simplicity).

cement paste prepared with the identical w/c ratio (0.3) [47]. The hydration degree is quite close to the results (63.0%) reported by Haecker et al. [39] using non-evaporable water content method. Due to the limitation of image resolution, pores smaller than 2 mm are not detectable and are mixed within the segmented solid phases [40–42]. Therefore, the total porosity derived from CT images is significantly lower than the theoretical total porosity predicted by Powers model (17.80%) [43] and mercury intrusion porosimetry (MIP) (17%) [44]. Thus, the segmented solid phases does not represent any single chemical composite in the HCP but several of them (e.g. calcium-silicate-hydrate gel, calcium hydroxide, ettringite and monosulfate, etc) mixed with smaller porosity. Fig. 8 shows a comparison between segmented material structure and its corresponding greyscale level image. With the

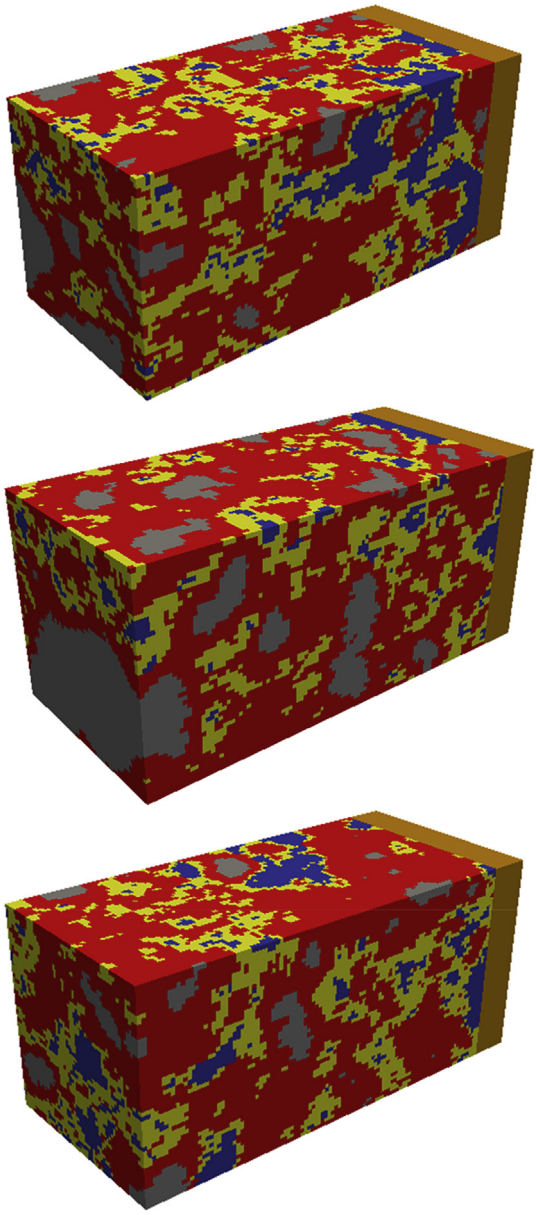

Fig. 9. Type I specimens with size of 220 μm × 100 μm × 100 μm (110 voxel × 50 voxel × 50 voxel, three specimens are shown for clarity).

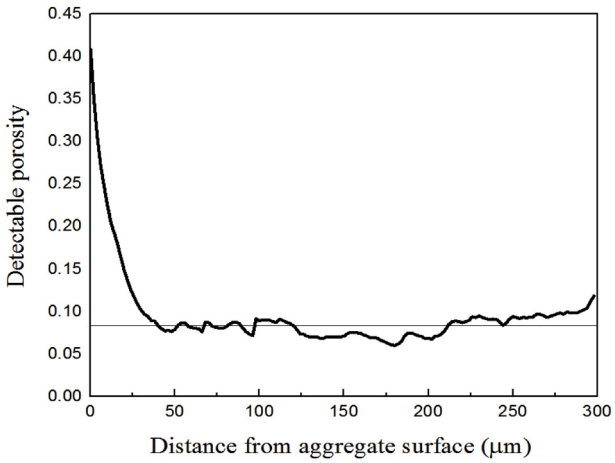

Fig. 10. Porosity profile of cement paste part in the ROI.

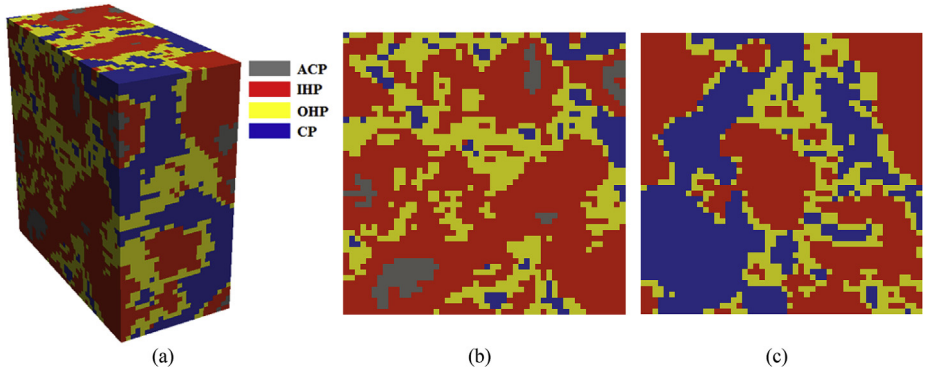

Fig. 11. Type II specimen with size of 50 μm × 100 μm × 100 μm (25 voxel × 50 voxel ×50 voxel): (a) side view; (b) view from the bulk cement paste side; (c) view from the aggregate side.

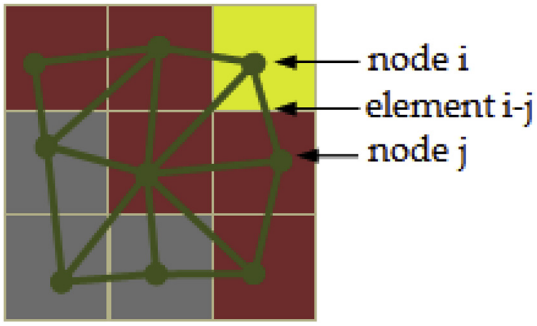

Fig. 12. An example of the overlay procedure for HCP, shown in 2D for simplicity, after [42].

Table 2
Lattice element types and their assumed mechanical properties [29,42].

Element type	Phase 1	Phase 2	Young's modulus (GPa)	Tensile strength (MPa)	Compressive strength (MPa)
A-A	ACP	ACP	99	683	6830
IHP	IHP	IHP	31	92	920
OHP	OHP	OHP	25	58	580
A-I	ACP	IHP	47	92	920
I-O	IHP	OHP	28	58	580
A-O	ACP	OHP	40	58	580
Ag-Ag	Aggregate	Aggregate	70	700	7000
Ag-I	Aggregate	IHP	–	–	–
Ag-O	Aggregate	OHP	–	–	–

approach proposed in this section, a multi-phase material structure can be segmented from these greyscale level based XCT images.

3.3. Digital specimen generation

Two types of digital specimens were extracted from the segmented voxel-based images for the fracture analysis. As shown in Fig. 9, the first one (Type I) has a cross-section of 100 μm × 100 μm and length of 220 μm consisting of 20 μm length of aggregate and 200 μm length of HCP. The features of this type specimen are assumed to be the same as the cantilever beam that is fabricated in Section 2.1. This enables the calibration of the fracture modelling in Section 4.2. In order to study the deviation of the mechanical properties of the investigated material as shown in the experiments, 10 digital specimens were randomly extracted. The second (Type II) is a pure ITZ specimen which is obtained by 'cutting' off the aggregate and bulk cement paste part from the Type I specimen. The thickness of this zone was determined by checking the porosity profile perpendicular to the interface in the ROI, see Fig. 10. It is clearly that with the position keeping away from the aggregate

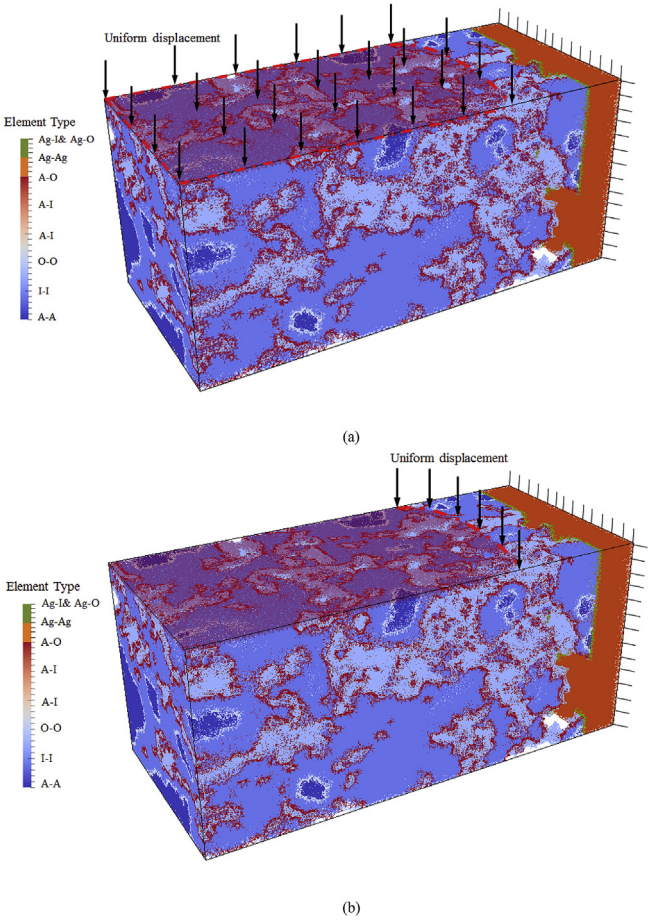

Fig. 13. Schematic illustration of the boundary configurations for the modelling of the cantilever under loading: (a) fully contacted with the indenter surface; (b) contacted with the edge of indenter.

Table 3
Calibrated mechanical properties of the lattice elements connecting aggregate and HCP.

Case number	Boundary configuration	Element type	Young's modulus (GPa)	Tensile strength (MPa)	Compressive strength (MPa)
1	Fully contacted	Ag-I	0.20	3.0	30
		Ag-O	0.16	2.5	25
2	Edge contacted	Ag-I	0.17	5.0	50
		Ag-O	0.14	4.2	42

Table 4
Mechanical properties of the pure ITZ derived from the simulated stress-strain curves of case 1.

No.	Young's modulus (GPa)	Tensile strength (MPa)	Fracture energy (J/m^2)
1	3.12	1.87	0.16
2	4.57	2.68	0.18
3	2.76	1.65	0.15
4	3.49	2.08	0.14
5	3.91	2.32	0.15
6	3.07	1.82	0.13
7	3.29	1.95	0.14
8	3.46	2.08	0.16
9	4.07	2.44	0.17
10	3.86	2.29	0.16
Average	3.560 ± 0.515	2.118 ± 0.298	0.154 ± 0.014

surface, the porosity decreases dramatically until reaches the average porosity (8.35%) of the bulk cement paste at around 50 μm. Therefore, 50 μm is regarded as the thickness of ITZ herein, which is in accordance with references [2,4,6]. The microstructure within this area was then extracted from Type I specimen to form the pure ITZ specimen as shown in Fig. 11. 10 Type II specimens were created to consider the deviation of the modelled micromechanical properties.

4. Deformation and fracture modelling

In this section, a discrete lattice fracture model, as described in Ref. [48], was used to predict the mechanical performance of the generated specimens. The type I specimen was used to calibrate the input local mechanical properties using the experimental measurements. After calibration, the fracture model was applied on Type II specimen to predict the mechanical properties of pure ITZ.

4.1. Modelling approach

In the discrete lattice fracture model, the material is discretised as a set of beam elements. A random triangular mesh [35] was used in current work. Then, a set of linear elastic analyses was performed by calculating the stress within each lattice element for an external boundary configuration following:

$$\sigma = \alpha_N \frac{N}{A} + \alpha_M \frac{\max(M_X, M_Y)}{W} \quad (2)$$

where A is the beam cross-sectional area, W the cross-sectional moment of resistance, α_N and α_M the normal force influence factor and the bending influence factor respectively. Their values are commonly adopted as 1.0 and 0.05, respectively. In every analysis step, loading is increased until the stress of one beam exactly meshes its prescribed strength. This beam is then removed from the mesh. The mesh is then updated and relaxed. This loading procedure is repeated until a predefined stopping criterion (e.g. load or displacement).

One of the advantages of such model is that the experimental observed material structure can be implemented directly. Herein, the material structure obtained in Section 3.3 was used. As shown in Fig. 12, for each lattice element, its mechanical properties are assigned according to the phase that it connects with. The elastic modulus of a lattice element i-j connecting phase i and j is determined using a Reuss (series) model as [42]:

$$\frac{2}{E_{ij}} = \frac{1}{E_i} + \frac{1}{E_j} \quad (3)$$

where E_i and E_j are elastic moduli corresponding to phase i and j, respectively. While for the strength (both compressive and tensile strength) of the lattice element i-j, it was assumed as the lower value in between phases i and j. In addition, it is worth mentioning that if either voxel i or voxel j is a pore voxel, no element is created representing the initial defect in the system.

For the elements that exist in the cement matrix, their mechanical properties have been calibrated and validated in the authors' previous

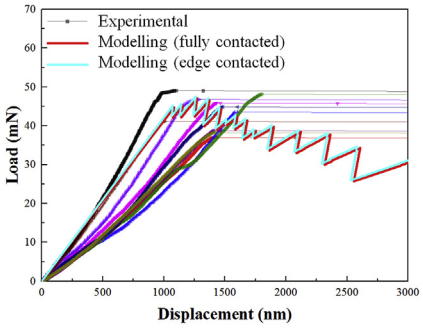

(a)

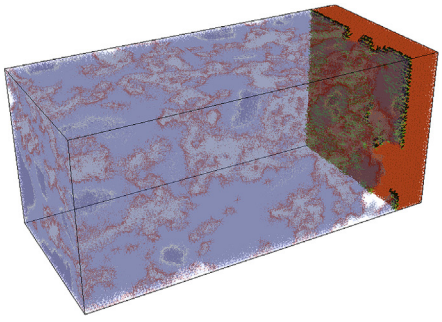

(b)

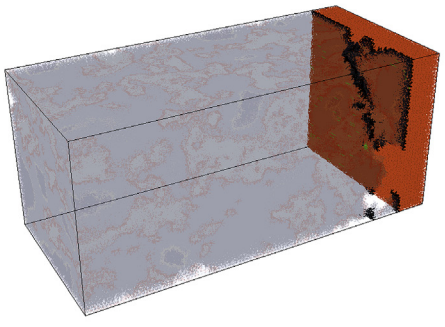

(c)

Fig. 14. (a) Comparison between simulated load-displacement curves and experimental results; (b) simulated crack patterns at peak load: (a); (c) simulated crack patterns at failure stage (black: crack, green: Ag-I and Ag-O). (For interpretation of the references to colour in this figure legend, the reader is referred to the Web version of this article.)

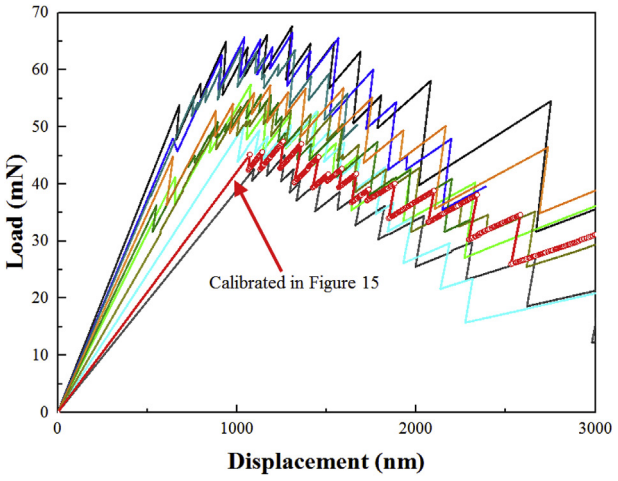

(a)

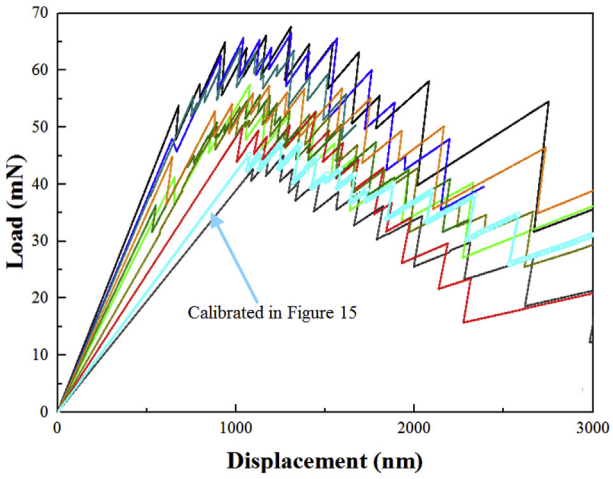

(b)

Fig. 15. Modelling results of 10 ITZ cantilever specimens under: (a) fully contacted boundary conditions (b) edge contacted boundary conditions.

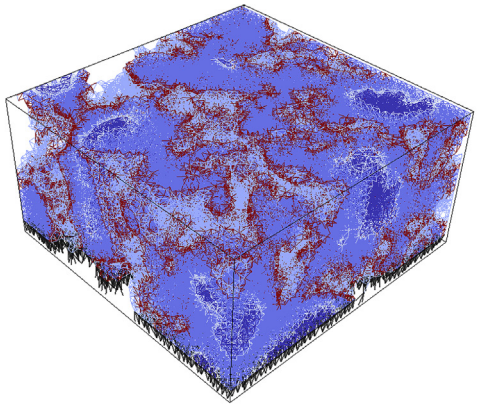

(a)

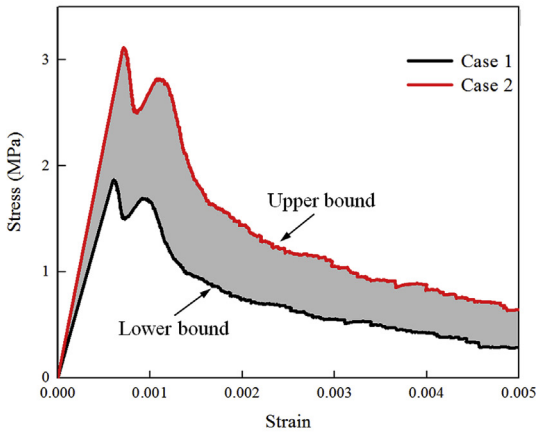

(b)

Fig. 16. Simulation results: (a) deformed mesh at failure for the ITZ specimen at the final stage (black colour denotes lattice elements that are damaged); (b) comparison between the simulated stress-strain curves of the ITZ specimen under uniaxial tension using different input parameters. (For interpretation of the references to colour in this figure legend, the reader is referred to the Web version of this article.)

work [42,49] and listed in Table 2. It is worth mentioning that, the resolution in Refs. [42,49] is identical with the current work. The calibrated local mechanical properties are depend on the resolution of digitalized microstructure: a lower resolution results in a coarser mesh, and lower local mechanical properties should be adopted since more larger pores and defects are homogenized in the domain represented by the element or voxel. With respect to the element within the aggregate, its elastic modulus is taken from Ref. [29] and listed in Table 4. Its tensile strength is assumed as 1/1000 of the modulus. The adopted strength/modulus ratio is larger than the one commonly observed at the meso-scale in order to consider the size effect [44,47,50]. Furthermore, because fracture happens at the cement paste part, the strength of the aggregate has no contribution to the mechanical response.

It is well known that a rather thin layer forms directly on the aggregate surface, typically a micron or so in thickness, including the products from any reaction that may happen between the aggregate and cement paste. These products contain mainly calcium silicate hydrate, calcium hydroxide and ettringite depending on the specimen preparation and the size of the aggregate [3,20,51–55]. This layer cannot be distinguished from the XCT images due to limited resolution and segmentation techniques. In order to take this layer into account, the elements that connect the solid phases in cement paste and the aggregate are generated, which has a comparable dimension with the thickness of the layer. For simplification, the mechanical properties of these elements are assumed proportional to the phases they connect with in HCP. In this way, the elastic moduli and strengths of these elements can be calibrated through inverse analysis using experimental measured load-displacement curves. Furthermore, it should be noticed that the element that connects the anhydrous cement particle and aggregate is removed from the mesh, as negligible bonding strength is expected for these two solid phases. This results in two types of interface elements (i.e. Ag-I, Ag-O, see Table 2) that are needed for the calibration.

4.2. Calibration and discussion

In this section, the discrete model was applied for the fracture analysis of the Type I specimen. As schematically shown in Fig. 13, a Type I digital specimen has been mapped to a lattice mesh. The end of the aggregate part was clamped. In the experimental test, due to the rotation of the cantilever beam, the contact area between the flat end tip and the cantilever beam decreases gradually from fully contacted to only the edge of the indenter with the deformation of beam increasing. However, such dynamic boundary configuration could not be implemented in the modelling. Two extreme boundary conditions as

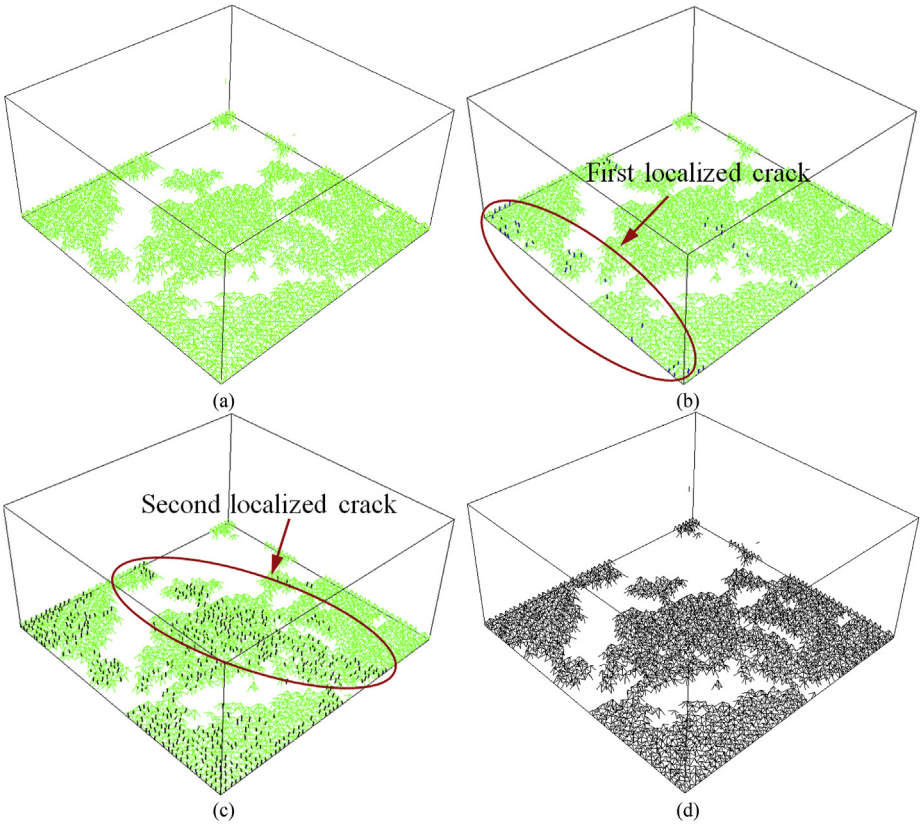

Fig. 17. Crack pattern of Type II specimens together with interface elements at different failure stage: (a) before loading; (b) first peak; (b) second peak; (c) final stage (black- broken interface element, green-unbroken interface element). (For interpretation of the references to colour in this figure legend, the reader is referred to the Web version of this article.)

shown in Fig. 13 are therefore adopted herein for the purpose of calibration. The fully contacted loading boundary condition was modelled by adding unit displacement at nodes within the dash line marked zone (Fig. 13a), while the edge contacted boundary condition is mimicked by applying unit displacement at the notes on the right side edge (Fig. 13b). Through a trial-and-error approach, satisfactory load-displacement curves were obtained when the values in Table 3 were adopted. As the fracture pattern for the simulated two boundaries are almost identical and a linear-elastic constitutive law is implemented for the local beam elements, the simulated load-displacement curves have similar shapes. Furthermore, the mechanical properties listed in Table 3 are rather low compared with the phases connected by the element in HCP. This tends to confirm the weak bonding between cement paste and aggregate. Fig. 14a presents the comparison between the simulated load displacement curve and the experimental ones. As mentioned above the experiments are not able to measure the post-peak behaviours, the comparison is only made in the pre-peak regime. Clearly, the simulation can reproduce the experimental measured results well in terms of the ascending slope and the peak load. The simulated fracture patterns at peak load and final stage are plotted in Fig. 14b and c. It is observed that, all the cracks happen in the interface (the weakest part of the specimen) until the peak load. At the failure stage, the HCP beam is debonded from the aggregate. It can be seen from Fig. 14c that almost all the interface elements are broken. While, the small amount unbroken interface element and the crack occurring in the HCP proves that there are some residual HCP left on the aggregate after the debonding. This is in accordance with the experimental observation.

The identical boundary configurations and input mechanical parameters are then used to model the fracture of the other 9 Type I specimens. The simulated load-displacement curves are shown in Fig. 15 for both boundary conditions. The load-displacement curves of all specimens consist of a linear ascending branch and a zig-zag descending branch. The zig-zag is a consequence of the use of a sequentially-linear procedure [56] in the model. After a beam element is removed from the lattice system, much less load is needed to break the next one(s) until an increasing load is required to continue further. This is comparable with a small propagation of a crack under a constant loading before the fracture process becomes stable again. Additionally, as expected, variations between individual specimens are observed due to the heterogeneity of the material structures.

4.3. Prediction of uniaxial tensile strength of ITZ

In order to predict the tensile strength and elastic modulus of the ITZ, microstructure of the pure ITZ as generated in Section 3.3 was used. A computational uniaxial tension test was conducted. In this case, one end of the material is clamped, and the nodal displacement is applied on the other. Neither lateral deformation nor nodal rotation is allowed at the two ends. For the elements in cement paste, parameters in Table 2 were used. With respect to the interface elements (i.e. Ag-I and Ag-O), the parameters that have been calibrated from two extreme boundary conditions (see Table 3) were used. This results in two sets of the input parameters which provide the two bounds (upper and lower) of the real stress-strain response of the ITZ. The same crack pattern is obtained for the two sets input parameters (see Fig. 16a, all the interface elements are broken), as the interface elements are the weakest elements in the system. The simulated stress-strain curves are compared in Fig. 16b. As expected, comparable stress-strain curves are observed for the two data sets. When implementing the interface elements calibrated from case 2, higher stress and stiffness are obtained at the same strain level. As the two data sets were fitted from two extreme boundary conditions, the real response of the tested ITZ specimen under uniaxial tension probably lies in between these two curves. Additionally, it is clear that the stress-strain curves have two stress peaks, while the first peak is higher than the second. These two peaks are attributed to the fixed boundary conditions for the computational uniaxial tensile test. In this case, the crack would first start in the weakest region. As the specimen boundaries are forced to remain parallel during crack

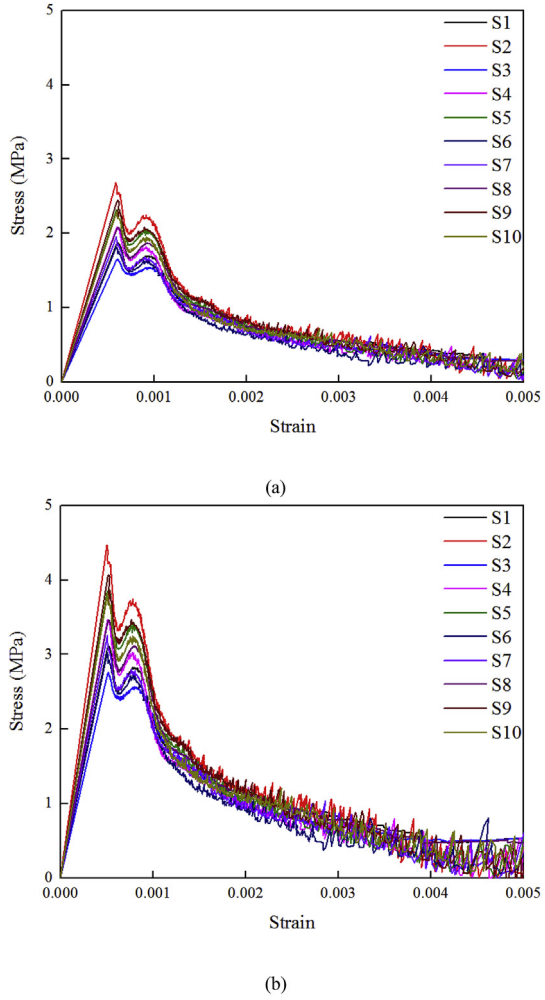

Fig. 18. Variations of simulated load-displacement responses due to the material structure heterogeneity: (a) case 1; (b) case 2.

Table 5
Mechanical properties of the pure ITZ derived from the simulated stress-strain curves of case 2.

No.	Young's modulus (GPa)	Tensile strength (MPa)	Fracture energy (J/m^2)
1	4.42	3.12	0.29
2	6.47	4.47	0.33
3	3.91	2.75	0.26
4	4.94	3.47	0.26
5	5.54	3.87	0.29
6	4.35	3.03	0.24
7	4.66	3.25	0.26
8	4.90	3.47	0.30
9	5.77	4.07	0.31
10	5.47	3.82	0.29
Average	5.040 ± 0.730	3.530 ± 0.498	0.283 ± 0.026

propagation, a closing bending moment is developed at the boundaries. Afterwards, further propagation of the first crack is arrested by the bending moments. Instead, the other part of the specimen starts to fracture [45]. One example is shown in Fig. 17 where the crack pattern at first, second peaks and the final stages are plotted together with the interface elements. Before crack happens (see Fig. 17a), a large number of defects already exist in the interface layer due to the high effective w/c ratio and the weak bound between anhydrous cement particles and aggregate. At the first peak (Fig. 17b), it seems like a crack starts localizing at the left side, while at the second peak (Fig. 17c), another

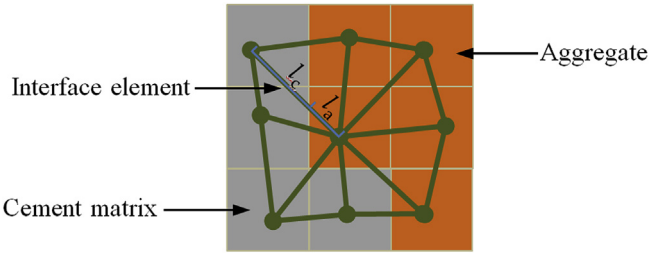

Fig. 19. Schematic view of the discrete lattice model at meso-scale.

crack going through the middle is observed. In the end, all the interface elements are broken, the specimen fails entirely, see Fig. 17d.

In order to show the variations of the mechanical properties of ITZ, 10 specimens were tested using both data sets. Their stress-strain curves are plotted in Fig. 18. All the stress-strain curves have two stress peaks because of the aforementioned reasons. Furthermore, the peaks of different specimens align almost at the same strain level when the same set mechanical properties of local elements are used. In terms of case 1, the first peak aligns around 0.0005, while the second aligns at around 0.001. At the strain level of 0.005, the stress almost reaches 0. Therefore, it is regarded as the final failure stage.

On the basis of the stress-strain curve, the strength, elastic modulus and fracture energy are derived and listed in Tables 4 and 5. Note that the fracture energy G_f is calculated from the post-peak part of the stress-strain curve as:

$$G_f = \int_{u1}^{u2} \sigma du \tag{4}$$

where σ is the stress, u the displacement, u_1 displacement at peak stress, u_2 the displacement at failure. As expected, these values are much lower compared with the bulk cement paste at the same length scale (strength: 25.78 MPa; elastic modulus 27.73 GPa; fracture energy: 9.94 J/m^2) [47]. When looking at the literature, the reported HCP-aggregate bonding strength varies a lot, even for the specified aggregate and w/c ratio of ordinary cement paste. For example, it is measured as 0.78 MPa by Zimbelmann [23] but reported by Ping and Beaudoin [57] as high as 4 MPa for the bonding strength between cement paste with 0.3 w/c ratio and "flat" quartzite surface at 28 days. This is partly because the bonding strength is significantly influenced by the geological properties of the aggregate, especially the surface roughness which is mainly determined by the pre-treatment process [58] and partly due to the specimen preparation method which has a considerable influence on internal stress in the boundary. Furthermore, it should be noted that a size effect occurs on the strength of cementitious material [44,47,50]. The most comparable experimental test that can be found in the literature is made by Jebli et al. [21] in which a uniaxial tension test has been conducted on a "sandwich" aggregate-cement-aggregate sample with a square cross-section of 10 mm, giving a estimation of the bonding strength as 1.6 MPa and an elastic modulus of 4.3 GPa for the composite. As the aggregate they used is limestone, lower bonding strength is expected for the quantize aggregate-cement at the meso-scale [58]. The modulus reported in Ref. [21] is a homogenised value with the aggregate and bulk cement paste, thus it is higher than the results for the pure ITZ as reported in the current study. It is reported in Ref. [13] that the Young's modulus of cement paste at distance of 20 μm away from the aggregate is around 2.2 MPa after 3 days hydration, which tends to confirm the simulated Young's modulus falls in the reasonable range.

5. General discussion

The predicted results have applications for the numerical fracture modelling of mortar or concrete at the meso-scale. At this scale, the interface properties between the aggregate and the bulk cement paste

matrix are important parameters, and it is concluded that global mechanical behaviour of the modelled material is dominated by the local mechanical properties of the interface [59]. Thus, the results reported in this work offer the reference for choosing the constitutive law of this feature in the numerical model. As the length of the ITZ determined in this work is 50 μm, it is perhaps too numerically expensive to represent it explicitly in most numerical models. As a consequence, homogenization is needed. An example is given in terms of a discrete lattice model. As shown in Fig. 19, in the lattice model, an interface element is generally used to connect aggregate and cement matrix and it always takes up also a piece of aggregate and a piece of cement paste matrix. Either linear elastic or multi-linear constitutive law can be assumed on the basis of the simulated stress-strain curves. The strength of this element at different stages can be taken directly from this work, while the modulus E_{int} can be "averaged" according to the length of its length l_{int} and position using a Reuss (series) model as:

$$\frac{l_{int}}{E_{int}} = \frac{l_c - l_{itz}}{E_c} + \frac{l_{itz}}{E_{itz}} + \frac{l_a}{E_a} \quad (5)$$

where l_c and E_c denote the length of the element in cement paste and the elastic modulus of cement paste; l_a and E_a are the length of the element in aggregate and the elastic modulus of the aggregate, l_{itz} and E_{itz} are the length and elastic modulus of the ITZ. In the end, it is worth mentioning that, for different types of model and purposes, different strategy should be considered on the basis of the assumptions in the simulation.

On the other hand, it is well-known that the mechanical properties of the interface between aggregate and cement paste are influenced by many factors, e.g. curing conditions and time, initial w/c of the mixture, aggregate type and surface roughness, etc. [2,4,10,58,60]. On the basis of the proposed testing and modelling approaches, the influence of these factors can be explicitly investigated at the micro metre length scale and up-scaled to the models at the meso-scale.

6. Conclusions

This work proposes an approach for the fracture testing and modelling of the ITZ at the micrometre length scale. The micrometre sized HCP-aggregate cantilever beams are fabricated and tested both experimentally and numerically. The experimentally measured load-displacement responses are used as benchmark for the calibration of the numerical model. After the calibration, the model can reproduce the experimental observations well including the variation and be applied to explain the experiments in detail. The calibrated model is further used to predict the fracture properties of the ITZ under uniaxial tension.

The model shows that the bonding between cement paste and aggregate is weak and a high porosity exists at the interface layer. Therefore, the micromechanical properties of the ITZ are much lower compared with the HCP at the same length scale. On the other hand, they are higher than the properties measured at the meso-scale due to the size effect.

The XCT scanning technique is able to capture porosity gradients of cement paste along the distance away from aggregate, which can be further used to distinguish the ITZ and bulk HCP from the matrix.

In the end, this work contributes to the multi-scale modelling of the concrete. The interface properties between cement paste and aggregate in the meso-scale model can be determined on the basis of the results presented in the current work.

More comprehensive work can be conducted on the basis of the proposed approaches to investigate the influence of different factors on the micromechanical properties of the ITZ. Through a multi-scale modelling framework, these influences can be explicitly visualized at meso-scale.

Acknowledgements

Hongzhi Zhang, Yading Xu, Yidong Gan would like to acknowledge the funding supported by China Scholarship Council under grant number 201506120067, 201708110187 and 201706130140 respectively. The authors would also like to acknowledge the help of Mr. Arjan Thijssen with XCT and ESEM experiments.

References

[1] T.T. Ghebrab, P. Soroushian, Mechanical properties of hydrated cement paste: development of structure-property relationships, Int. J. Concr. Struct. Mater. 4 (2010) 37–43.
[2] L. Struble, J. Skalny, S. Mindess, A review of the cement-aggregate bond, Cem. Concr. Res. 10 (1980) 277–286.
[3] B. Barnes, S. Diamond, W. Dolch, The contact zone between Portland cement paste and glass "aggregate" surfaces, Cem. Concr. Res. 8 (1978) 233–243.
[4] K.L. Scrivener, A.K. Crumbie, P. Laugesen, The interfacial transition zone (ITZ) between cement paste and aggregate in concrete, Interface Sci. 12 (2004) 411–421.
[5] S. Diamond, J. Huang, The ITZ in concrete–a different view based on image analysis and SEM observations, Cem. Concr. Compos. 23 (2001) 179–188.
[6] A. Delagrave, J. Bigas, J. Ollivier, J. Marchand, M. Pigeon, Influence of the interfacial zone on the chloride diffusivity of mortars, Adv. Cem. Base Mater. 5 (1997) 86–92.
[7] B. Nyame, Permeability of normal and lightweight mortars, Mag. Concr. Res. 37 (1985) 44–48.
[8] A. Principigallo, K. van Breugel, G. Levita, Influence of the aggregate on the electrical conductivity of Portland cement concretes, Cem. Concr. Res. 33 (2003) 1755–1763.
[9] Q.-f. Liu, G.-l. Feng, J. Xia, J. Yang, L.-y. Li, Ionic transport features in concrete composites containing various shaped aggregates: a numerical study, CmpSt 183 (2018) 371–380.
[10] T. Akçaoğlu, M. Tokyay, T. Çelik, Effect of coarse aggregate size and matrix quality on ITZ and failure behavior of concrete under uniaxial compression, Cem. Concr. Compos. 26 (2004) 633–638.
[11] G. Ramesh, E. Sotelino, W. Chen, Effect of transition zone on elastic moduli of concrete materials, Cem. Concr. Res. 26 (1996) 611–622.
[12] A.R. Mohamed, W. Hansen, Micromechanical modeling of crack-aggregate interaction in concrete materials, Cem. Concr. Compos. 21 (1999) 349–359.
[13] F. Grondin, M. Matallah, How to consider the Interfacial Transition Zones in the finite element modelling of concrete? Cem. Concr. Res. 58 (2014) 67–75.
[14] S. Zhang, C. Zhang, L. Liao, C. Wang, Numerical study of the effect of ITZ on the failure behaviour of concrete by using particle element modelling, Constr. Build. Mater. 170 (2018) 776–789.
[15] S.-M. Kim, R.K. Abu Al-Rub, Meso-scale computational modeling of the plastic-damage response of cementitious composites, Cem. Concr. Res. 41 (2011) 339–358.
[16] X.F. Wang, Z.J. Yang, J.R. Yates, A.P. Jivkov, C. Zhang, Monte Carlo simulations of mesoscale fracture modelling of concrete with random aggregates and pores, Constr. Build. Mater. 75 (2015) 35–45.
[17] L. Snozzi, A. Caballero, J.-F. Molinari, Influence of the meso-structure in dynamic fracture simulation of concrete under tensile loading, Cem. Concr. Res. 41 (2011) 1130–1142.
[18] G. Lilliu, J.G. van Mier, 3D lattice type fracture model for concrete, Eng. Fract. Mech. 70 (2003) 927–941.
[19] B. Šavija, J. Pacheco, E. Schlangen, Lattice modeling of chloride diffusion in sound and cracked concrete, Cem. Concr. Compos. 42 (2013) 30–40.
[20] K.L. Scrivener, P.L. Pratt, Characterization of interfacial microstructure, Interfacial Trans. Zone Concr. 2 (1996) 3–18.
[21] M. Jebli, F. Jamin, E. Malachanne, E. Garcia-Diaz, M.S. El Youssoufi, Experimental characterization of mechanical properties of the cement-aggregate interface in concrete, Constr. Build. Mater. 161 (2018) 16–25.
[22] T. Thomas, F.O. Slate, Tensile bond strength between aggregate and cement paste or mortar, J. Proc. (1963) 465–486.
[23] R. Zimbelmann, A contribution to the problem of cement-aggregate bond, Cem. Concr. Res. 15 (1985) 801–808.
[24] J. Wang, A. Maji, Experimental studies and modeling of the concrete/rock interface, ACI Spec. Publ. Interface Fract. Bond 156 (1994) 45–68.
[25] E. Tschegg, H. Rotter, P. Roelfstra, U. Bourgund, P. Jussel, Fracture mechanical behavior of aggregate–cement matrix interfaces, J. Mater. Civ. Eng. 7 (1995) 199–203.
[26] K. Alexander, Strength of the cement aggregate bond, J. Proc. (1959) 377–390.
[27] C. Perry, J. Gillott, The influence of silica fume on the strength of the cement-aggregate bond, Spec. Publ. 156 (1995) 191–212.
[28] W. Dong, Z. Wu, X. Zhou, N. Wang, G. Kastiukas, An experimental study on crack propagation at rock-concrete interface using digital image correlation technique, Eng. Fract. Mech. 171 (2017) 50–63.
[29] M. Hassanzadeh, Fracture mechanical properties of rocks and mortar/rock interfaces, MRS Online Proc. Libr. Arch. (1994) 370.
[30] O. Buyukozturk, B. Hearing, Crack propagation in concrete composites influenced by interface fracture parameters, Int. J. Solids Struct. 35 (1998) 4055–4066.
[31] S. Caliskan, Aggregate/mortar interface: influence of silica fume at the micro-and macro-level, Cem. Concr. Compos. 25 (2003) 557–564.
[32] K. Mitsui, Z. Li, D. Lange, S. Shah, 13 A study of properties of the paste-aggregate interface, Interfac. Cementitious Compos. (1993) 119.

[33] A. Abu-Tair, S. Rigden, E. Burley, Testing the bond between repair materials and concrete substrate, Mater. J. 93 (1996) 553–558.
[34] E. Garboczi, Stress, displacement, and expansive cracking around a single spherical aggregate under different expansive conditions, Cem. Concr. Res. 27 (1997) 495–500.
[35] D.P. Bentz, E.J. Garboczi, Computer Modelling of Interfacial Transition Zone: Microstructure and Properties, (1999).
[36] Z. Sun, E.J. Garboczi, S.P. Shah, Modeling the elastic properties of concrete composites: experiment, differential effective medium theory, and numerical simulation, Cem. Concr. Compos. 29 (2007) 22–38.
[37] J. Němeček, V. Králík, V. Šmilauer, L. Polívka, A. Jäger, Tensile strength of hydrated cement paste phases assessed by micro-bending tests and nanoindentation, Cem. Concr. Compos. 73 (2016) 164–173.
[38] S.J. Chen, W.H. Duan, Z.J. Li, T.B. Sui, New approach for characterisation of mechanical properties of cement paste at micrometre scale, Mater. Des. 87 (2015) 992–995.
[39] R. Shahrin, C.P. Bobko, Characterizing strength and failure of calcium silicate hydrate aggregates in cement paste under micropillar compression, J. Nanomech. Micromech. 7 (2017) 06017002.
[40] H. Zhang, B. Šavija, E. Schlangen, Combined experimental and numerical study on micro-cube indentation splitting test of cement paste, Eng. Fract. Mech. 199 (2018) 773–786.
[41] H. Zhang, B. Šavija, S.C. Figueiredo, E. Schlangen, Experimentally validated multi-scale modelling scheme of deformation and fracture of cement paste, Cem. Concr. Res. 102 (2017) 175–186.
[42] H. Zhang, B. Šavija, S. Chaves Figueiredo, M. Lukovic, E. Schlangen, Microscale testing and modelling of cement paste as basis for multi-scale modelling, Materials 9 (2016) 907.
[43] Y. Gan, H. Zhang, B. Šavija, E. Schlangen, K. van Breugel, Static and fatigue tests on cementitious cantilever beams using nanoindenter, Micromachines 9 (2018) 630.
[44] H. Zhang, B. Šavija, Y. Xu, E. Schlangen, Size effect on splitting strength of hardened cement paste: experimental and numerical study, Cem. Concr. Compos. 94 (2018) 264–276.
[45] J.G. Van Mier, Fracture Processes of Concrete, CRC press, 2017.
[46] H. Zhang, B. Šavija, M. Luković, E. Schlangen, Experimentally informed micromechanical modelling of cement paste: an approach coupling X-ray computed tomography and statistical nanoindentation, Compos. B Eng. 157 (2019) 109–122.
[47] H. Zhang, B. Šavija, E. Schlangen, Towards understanding stochastic fracture performance of cement paste at micro length scale based on numerical simulation, Constr. Build. Mater. 183 (2018) 189–201.
[48] E. Schlangen, E. Garboczi, Fracture simulations of concrete using lattice models: computational aspects, Eng. Fract. Mech. 57 (1997) 319–332.
[49] H. Zhang, B. Šavija, E. Schlangen, Combined Experimental and Numerical Study on Micro-cube Indentation Splitting Test of Cement Paste, Engineering Fracture Mechanics, 2018.
[50] Z.P. Bažant, S.-D. Pang, Activation energy based extreme value statistics and size effect in brittle and quasibrittle fracture, J. Mech. Phys. Solids 55 (2007) 91–131.
[51] C.Z. Yuan, W.J. Guo, Bond between marble and cement paste, Cem. Concr. Res. 17 (1987) 544–552.
[52] X. Zhang, G. Groves, S. Rodger, The microstructure of cement aggregate interfaces, MRS Online Proc. Libr. Arch. (1987) 114.
[53] P.J. Monteiro, C.P. Ostertag, Analysis of the aggregate-cement paste interface using grazing incidence X-ray scattering, Cem. Concr. Res. 19 (1989) 987–988.
[54] X. Ping, J. Beaudoin, R. Brousseau, Flat aggregate-portland cement paste interfaces, I. electrical conductivity models, Cem. Concr. Res. 21 (1991) 515–522.
[55] X. Ping, J.J. Beaudoin, R. Brousseau, Effect of aggregate size on transition zone properties at the portland cement paste interface, Cem. Concr. Res. 21 (1991) 999–1005.
[56] E. Schlangen, Experimental and Numerical Analysis of Fracture Processes in Concrete, Delft University of Technology, Delft University of Technology, Delft, The Netherlands, 1993.
[57] X. Ping, J. Beaudoin, Effects of transition zone microstructure on bond strength of aggregate-portland cement paste interfaces, Cem. Concr. Res. 22 (1992) 23–26.
[58] W. Tasong, C. Lynsdale, J. Cripps, Aggregate-cement paste interface. II: influence of aggregate physical properties, Cem. Concr. Res. 28 (1998) 1453–1465.
[59] W. Trawiński, J. Tejchman, J. Bobiński, A three-dimensional meso-scale modelling of concrete fracture, based on cohesive elements and X-ray μCT images, Eng. Fract. Mech. 189 (2018) 27–50.
[60] W.A. Tasong, C.J. Lynsdale, J.C. Cripps, Aggregate-cement paste interface: Part I. Influence of aggregate geochemistry, Cem. Concr. Res. 29 (1999) 1019–1025.